Journal of Geophysical Research: Solid Earth

RESEARCH ARTICLE
10.1002/2017JB015262

Special Section:
Magnetism in the Geosciences - Advances and Perspectives

Unusual Magnetic Properties of Sedimentary Pyrrhotite in Methane Seepage Sediments: Comparison With Metamorphic Pyrrhotite and Sedimentary Greigite

Chorng-Shern Horng[1]

[1]Institute of Earth Sciences, Academia Sinica, Taipei, Taiwan

Abstract Interpretation of the paleomagnetic and environmental signals carried by magnetic iron sulfide minerals depends on the ability to diagnose their magnetic properties and to recognize their origin. Greigite (Fe_3S_4) and hexagonal pyrrhotite (with variable composition between Fe_9S_{10} and $Fe_{11}S_{12}$) often form authigenically in sulfidic and methanic sedimentary environments, whereas monoclinic pyrrhotite (Fe_7S_8) occurs widely in igneous and metamorphic rocks so that erosion of such rocks can give rise to deposition of detrital pyrrhotite in sediments. In this study, low- and high-field, and low-, room temperature, and high-temperature magnetization data are presented to demonstrate that these magnetic iron sulfide minerals have contrasting magnetic properties that enable their identification, particularly when assisted by mineralogical characterizations. The results presented here should have wide applicability in sedimentary magnetic studies.

Key Points:
- Authigenic pyrrhotite formation via diagenetic processes has been reported increasingly in gas hydrate/methane venting areas
- Sedimentary authigenic pyrrhotite has a hexagonal (3 T) structure, rather than the conventionally assumed monoclinic (4 M) type
- Sedimentary hexagonal pyrrhotite has contrasting magnetic properties compared with metamorphic monoclinic pyrrhotite and sedimentary greigite

Supporting Information:
- Supporting Information S1
- Data Set S1

Correspondence to:
C.-S. Horng,
cshorng@earth.sinica.edu.tw

Citation:
Horng, C.-S. (2018). Unusual magnetic properties of sedimentary pyrrhotite in methane seepage sediments: Comparison with metamorphic pyrrhotite and sedimentary greigite. *Journal of Geophysical Research: Solid Earth*, *123*, 4601–4617. https://doi.org/10.1002/2017JB015262

Received 22 NOV 2017
Accepted 18 MAR 2018
Accepted article online 23 MAR 2018
Published online 22 JUN 2018

1. Introduction

Greigite (Fe_3S_4) and monoclinic pyrrhotite (Fe_7S_8) are the two most important magnetic iron sulfide minerals. Understanding their magnetic properties is important in paleomagnetism, rock magnetism, and environmental magnetism. Greigite has a cubic inverse spinel structure and forms either through bacterial biomineralization, as an authigenic product during sulfidic or methanic diagenesis in marine or lacustrine sediments or in hydrothermal settings at temperatures up to 180°C (Roberts et al., 2011). Monoclinic pyrrhotite belongs to a nonstoichiometric iron monosulfide group with various chemical compositions ($Fe_{1-x}S$, x = 0–0.125) and crystal structures, including hexagonal polymorphs, and occurs widely in hydrothermal, igneous, metamorphic, and extraterrestrial rocks (Rochette et al., 2001, 2003; Wang & Salveson, 2005). Pyrrhotite has been regarded as rare in sediments because of its instability during transportation in oxidizing environments, and until now it does not receive much attention. However, pyrrhotite has been reported increasingly in sulfidic and methanic marine sediments and can be derived either from erosion of pyrrhotite-bearing rocks on land, followed by rapid transportation and deposition (Horng et al., 2012; Horng & Huh, 2011; Horng & Roberts, 2006), or it can form during sediment diagenesis (Dinarès-Turell & Dekkers, 1999; Kars & Kodama, 2015; Larrasoaña et al., 2007; Roberts, 2015; Rudmin et al., 2018; van Dongen et al., 2007; Weaver et al., 2002), usually in offshore continental margins or gas hydrate areas. The two source types can be discriminated because the former has detrital textures, whereas the latter generally forms as interlocking plates within nodules (Horng & Roberts, 2006; Roberts, 2015).

In contrast to monoclinic pyrrhotite, which is ferrimagnetic, hexagonal pyrrhotite (e.g., Fe_9S_{10} or $Fe_{11}S_{12}$) is antiferromagnetic at room temperature (O'Reilly et al., 2000). Thus, magnetic pyrrhotite in sediments has been assumed routinely to be monoclinic (Roberts, 2015), although the crystal structure of pyrrhotite has not been investigated widely for geological pyrrhotite occurrences. This assumption is tested in the present study.

In the region offshore of southwestern Taiwan, bottom simulating seismic reflectors indicate the presence of gas hydrate reservoirs beneath the seafloor and methane gas plumes bubbling up from the seafloor have been observed frequently from seismic reflection and CHIRP sonar data, respectively (Chen et al., 2014; Liu et al., 2006). Marine sediments in the region, particularly near submarine ridges, usually have anomalously high methane gas contents (Chuang et al., 2006) and contain authigenic iron sulfide minerals (i.e., greigite, pyrrhotite, and pyrite; Horng & Chen, 2006; Lim et al., 2011), which indicate an intimate relationship between iron sulfide formation and methane seepage in the sediments. In addition to the common occurrence of

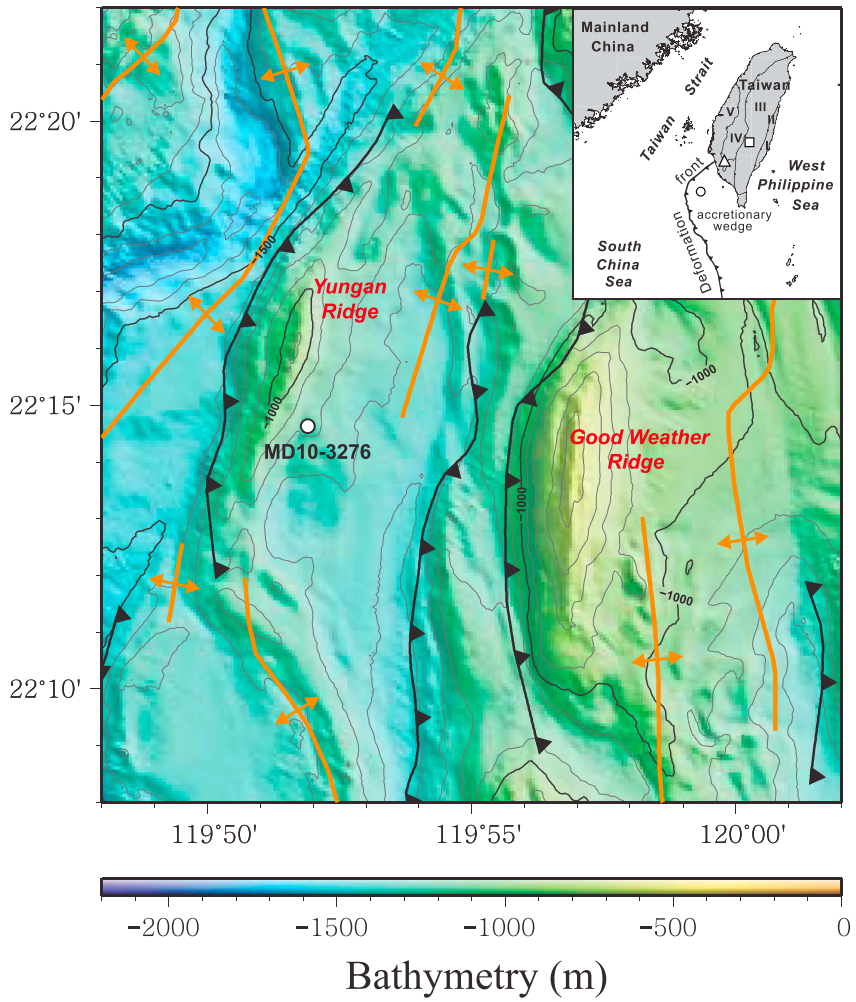

Figure 1. Location map and geological setting of marine sediment core MD10-3276 recovered from the Yungan Ridge offshore of southwestern Taiwan. Locations are indicated in the inset for the marine core (○), and two land sections (M11 and EJE) along the southern cross-island highway (□) and on the eastern part of the Erhjen-chi river section (△) where metamorphic pyrrhotite and sedimentary greigite samples were obtained for this study, respectively (see Horng & Roberts, 2006; Jiang et al., 2001). The five structural units of Taiwan are indicated: (I) Coastal Range, (II) Longitudinal Valley, (III) Central Range, (IV) Western Foothills, and (V) Coastal Plain.

authigenic iron sulfide minerals in submarine areas offshore of southwestern Taiwan, pyrrhotite in low-grade metamorphic rocks and greigite in Plio-Pleistocene marine mudstones are widespread, respectively, in the Central Mountain Range and southwestern Foothills of Taiwan (Horng et al., 2012; Horng & Roberts, 2006; Jiang et al., 2001). The presence of different iron sulfide minerals in offshore sediments and onshore rocks, thus, provides an opportunity to compare their magnetic properties. In this study, measurements of room temperature, low-temperature (5–300 K), and high-temperature (300–700 K) magnetic properties, combined with petrographic and mineralogical analyses, were carried out to understand the magnetic properties of authigenic sedimentary pyrrhotite from marine methane seepage environments and to compare them with those of metamorphic pyrrhotite and sedimentary greigite.

2. Geological Setting and Samples

Authigenic pyrrhotite nodules were obtained from core MD10-3276 (which recovered sediment to depths of 25.58 m below sea floor) from the eastern flank of Yungan Ridge (22.2438°N, 119.8650°E, Figure 1) at a water

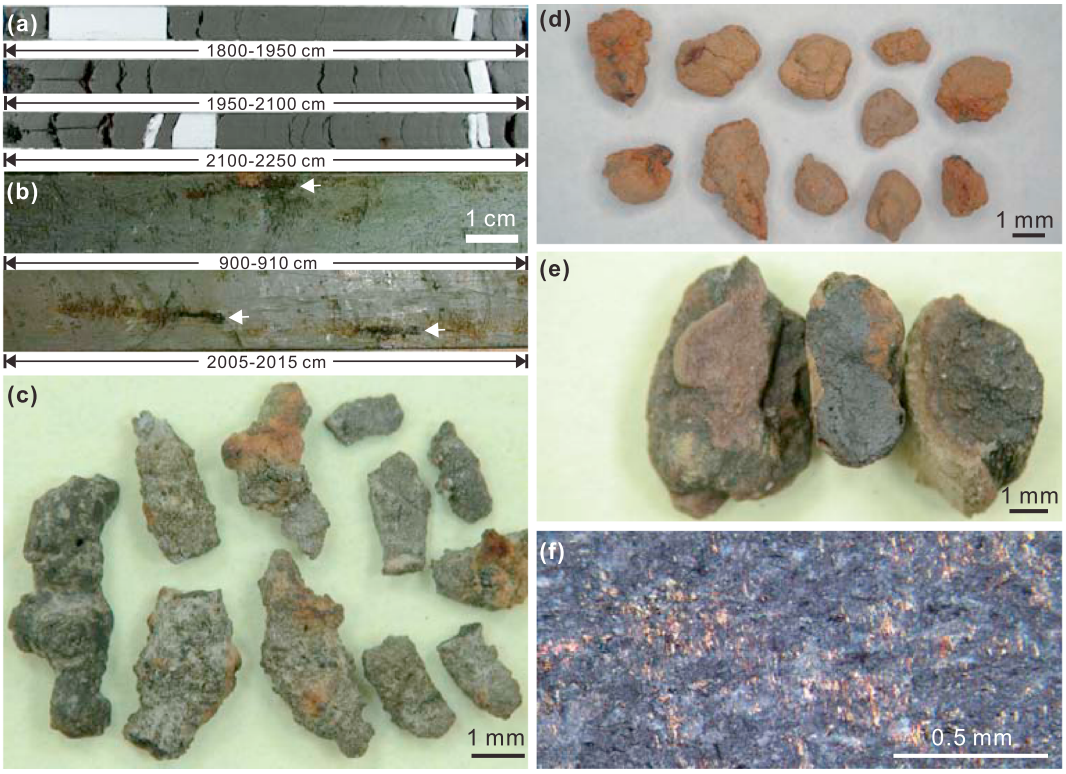

Figure 2. Images of samples analyzed in this study, taken by camera (a and b) or observed with optical microscope under reflected light (c–f), respectively. (a) Images of small cracks or large gaps in the lower part of core MD10-3276 (depths from 10.00 to 25.58 m) due to methane gas escape. Large gaps are filled with polystyrene blocks. (b) Black or earthy yellow speckles in the sediment core are indicated with white arrows. (c) Image of diagenetic nodules from the speckled sediments (4.90-m depth in core). (d) Nodules from 20.08 m, which mainly consist of goethite (α-FeOOH; see Figure 3e). (e) Greigite nodules from mudstone in the Plio-Pleistocene EJE section. (f) Abundant reddish-brown pyrrhotite grains in a phyllite from the M11 metamorphic section from the Taiwan Central Range.

depth of 1171 m during a cruise of the R/V *Marion Dufresne* in 2010. Yungan Ridge is located within an accretionary wedge complex that contains many actively growing faults and folds on the Philippine Sea plate, which overrides the subducting South China Sea plate (Lin et al., 2008; Figure 1 inset). This setting also contains several submarine canyon-channel systems. Fractures in the sediments provide conduits for upward methane gas migration, which results in high sediment methane contents (100–10,000 μl/L; Chiu et al., 2006; Chuang et al., 2006).

Core MD10-3276 consists of fine-grained mud with small cracks or large gaps in the lower part of the core (Figure 2a). Cracks and gaps in the sediment likely resulted from gas expansion and escape during coring and core splitting. Numerous black or earthy yellow speckles also occur throughout the core (Figure 2b). The speckled sediments contain submillimeter- to millimeter-scale nodules (Figures 2c and 2d). Optical microscopic observations of polished nodule surfaces under reflected light reveal that their interiors are filled with pyrite and other fine-grained mineral aggregates with an oxidized surface crust. The presence of pyrite indicates that the regions in which nodules formed experienced sulfidic conditions (Roberts, 2015). Most of the nodules have detectable magnetizations, and magnetic minerals can be separated with a rare earth magnet for magnetic and mineralogical investigations.

Metamorphic pyrrhotite and sedimentary greigite samples were collected along the M11 (approximately 23.2653°N, 120.9546°E) and EJE (approximately 22.8884°N, 120.4013°E) sections in Taiwan (Figure 1 inset), where low-grade metamorphic rocks (e.g., phyllites and schists) and Plio-Pleistocene marine mudstones contain pyrrhotite and greigite, respectively (Horng et al., 2012; Horng & Roberts, 2006; Jiang et al., 2001). Representative sedimentary greigite nodules and metamorphic pyrrhotite samples are shown in Figures 2e and 2f.

3. Methods

Magnetic authigenic nodules were taken from core MD10-3276 at depths of 4.90 m, 7.22 m, 11.42 m, 12.02 m, and 20.08 m. In general, the nodules are large enough (>1 mm; Figures 2c and 2d) to allow multiple analyses. X-ray diffraction (XRD) analysis was performed first after powdering to <10 μm, to identify mineral components using a Wiggler X-ray beamline (BL17A1) at the National Synchrotron Radiation Research Center, Taiwan (wavelength λ = 1.32090 Å). Synchrotron-based XRD analysis provides several important advantages over conventional laboratory-based XRD analysis. The high intensity of the synchrotron X-ray beam means that analyses are rapid (several minutes), peaks are sharper and better resolved with less overlap with neighboring peaks because of the use of an area detector rather than a point detector, and better signal-to-noise ratios are obtained so that minerals with concentrations <0.1% can be detected (this limit depends on scattering and the crystallinity of the material analyzed). For the present study, these aspects enable precise identification of magnetic minerals within iron sulfide nodules. To understand textural relationships among the XRD-identified minerals, petrographic observations were made on polished nodules using a JEOL JSM-6360LV scanning electron microscope (SEM) operated at 15 keV with 18-nA acceleration voltage. Chemical compositions of minerals were determined using an Oxford Instruments Ltd. INCA-300 X-ray energy dispersive spectrometer (EDS) attached to the SEM.

Low-field magnetic susceptibility (χ), saturation remanent magnetization (M_{rs}), saturation magnetization (M_s), coercivity (B_c), coercivity of remanence (B_{cr}), and S ratio (i.e., $-IRM_{-0.3T}/M_{rs}$; King & Channell, 1991) were measured at room temperature and a low-temperature saturation isothermal remanent magnetization (SIRM) was measured at low temperatures (5–300 K). Nodule samples were weighed with a precision of 0.1 mg and magnetic parameters are expressed in mass-specific terms. Magnetic hysteresis parameters (M_{rs}, M_s, B_c, and B_{cr}), initial slopes at low fields (0–0.03 T), and S ratios were measured on weighed specimens using a Princeton Measurements Corporation vibrating sample magnetometer (VSM) to maximum fields of ±1.0 T. χ values for specimens were derived from the initial slopes of magnetic hysteresis loops at low fields by subtracting the high-field slope (0.8–1.0 T). Details of the method used to calculate χ values are provided in the supporting information. First-order reversal curves (FORCs; Pike et al., 1999; Roberts et al., 2000) were also measured for nodules (1-T saturating field, average time 250 ms, and number of FORCs 140), and FORC diagrams were processed using the algorithm of Harrison and Feinberg (2008).

Low-temperature magnetic measurements were made on the same specimens using a Quantum Design SQUID (Superconducting Quantum Interference Device) VSM. Specimens were cooled from room temperature to 5 K in zero field. At 5 K, a 5-T direct current field was applied and was then switched off to impart a saturation isothermal remanent magnetization (SIRM). SIRM curves were measured to 300 K at a heating rate of 3 K/min to determine whether specimens undergo the low-temperature Besnus magnetic transition in pyrrhotite during zero-field warming (Besnus & Meyer, 1964; Dekkers et al., 1989; Fillion & Rochette, 1988; Rochette et al., 1990).

Magnetic minerals were also separated from nodule-bearing host sediments. Sediments were sieved with a 63-μm sieve to separate authigenic nodules. A rare earth magnet was then used to extract magnetic particles from the <63-μm sediment slurry. XRD, SEM, and SQUID VSM measurements were made on the extracts to characterize magnetic minerals and their low-temperature magnetic properties.

Magnetic hysteresis and FORC measurements were also made on metamorphic pyrrhotite grains and sedimentary greigite nodules. Metamorphic pyrrhotite grains (labeled MPoEx) were obtained by gently grinding pyrrhotite-bearing metamorphic rocks (Figure 2f) into powders and extracting them from a slurry with a rare earth magnet. Pyrrhotite extracts were purified magnetically several times and a small portion was used for synchrotron XRD crystal structure analysis. The remaining sample was subdivided into five fractions (63–125, 20–38, 10–20, 2–10, and <2 μm) with sieves and membrane filters. Sedimentary greigite nodules (labeled SGrN; Figure 2e) were excavated from the soft mudstone and were cleaned in an ultrasonic bath. Bulk samples from pyrrhotite- and greigite-bearing rocks (labeled MPoRx and SGrRx; N = 70 and 85, respectively) were also subjected to room temperature hysteresis analysis. Thermomagnetic measurements were conducted on sedimentary nodules from core MD10-3276, greigite nodules from the EJE section, and metamorphic pyrrhotite-bearing rocks from the M11 section using a SQUID VSM. Samples were subjected to a 3-T direct current field and were heated under vacuum ($<50 \times 10^{-3}$/torr) from 300 to 700 K (i.e., 27 to 427°C) and were then cooled to room temperature at 3 K/min.

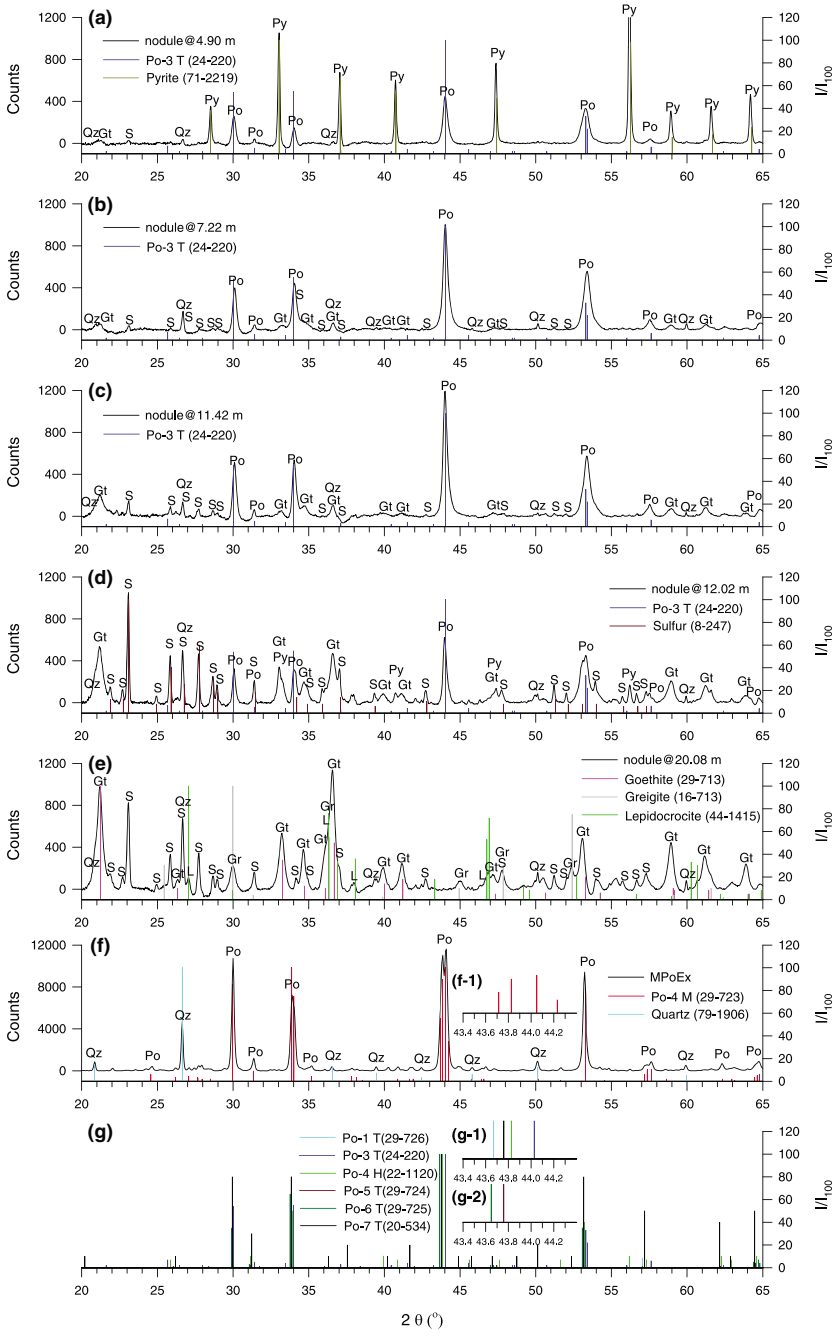

Figure 3. Mineralogical characterization of samples analyzed in this study. (a–e) X-ray diffraction patterns (counts versus 2θ angle) and mineral components (Po = pyrrhotite; Py = pyrite; S = sulfur; Gt = goethite; Gr = greigite; L = lepidocrocite; Qz = quartz) for sedimentary authigenic nodules from different depths (Figure 3a, 4.90 m; Figure 3b, 7.22 m; Figure 3c, 11.42 m; Figure 3d, 12.02 m; Figure 3e, 20.08 m) in core MD10-3276. (f) X-ray diffraction pattern and mineral components (Po = pyrrhotite; Qz = quartz) for a magnetic extract from a metamorphic pyrrhotite-bearing rock (phyllite, M11 section). Minerals were identified using the powder diffraction file (PDF) from the International Centre for Diffraction Data (Mineral Powder Diffraction File Databook, 1993). PDF numbers (#) of minerals are as follows: #24–220 (Po-3 T), #71–2219 (Py), #8–247 (S), #29–713 (Gt), #16–713 (Gr), #44–1415 (L), #29–723 (Po-4 M), and #79–1906 (Qz); their diffraction positions and relative intensities are shown with vertical lines with respect to the largest peak (I/I_{100}), respectively. (g) Peak positions and relative intensities for six polytypes of hexagonal pyrrhotite. PDF numbers: #29–726 (Po-1 T), #24–220 (Po-3 T), #22–1120 (Po-4 H), #29–724 (Po-5 T), #29–725 (Po-6 T), and #20–534 (Po-7 T). Diffraction positions are indicated in the insets in (f) and (g) (43.4–44.4° of 2θ) for the strongest peaks for monoclinic pyrrhotite (f-1: 4 M) and six hexagonal pyrrhotite samples (g-1: 1 T, 3 T, 4 H, and 7 T; g-2: 5 T and 6 T). Only Po-3 T with a single, most intense reflection peak at ~44.03° fits the pyrrhotite diffraction patterns from the authigenic pyrrhotite-bearing nodules (Figures 3a–3d).

4. Results

4.1. Mineral Components in Authigenic Nodules

Synchrotron radiation XRD analysis on authigenic nodules collected at five sediment depths of 4.90, 7.22, 11.42, 12.02, and 20.08 m from core MD10-3276 provides clear diffraction patterns for detailed mineral identification. Results, after transforming the original 2θ angles (λ = 1.32090 Å) to those based on conventional Cu Kα radiation (λ = 1.54056 Å) and background subtraction at lower angles using WinPLOTR software, are shown in Figures 3a–3e. Pyrrhotite is common, and minor quartz is generally present in nodules from the upper four studied levels (i.e., 4.90, 7.22, 11.42, and 12.02 m). Other iron sulfide and oxide minerals also occur in variable concentrations. For example, pyrite (FeS_2) is abundant in the nodule from 4.90 m, but it is absent or rare in the other three samples. In contrast, goethite (α-FeOOH) and elemental S are increasingly abundant from upper to lower levels. However, the nodule from 20.08 m (Figure 3e) does not contain pyrrhotite but consists mainly of goethite and S with small greigite and lepidocrocite (γ-FeOOH) contents. The coexistence of iron oxide and sulfide minerals in variable concentrations in the nodules implies that sediments from core MD10-3276 have undergone temporal variation between sulfidic and oxic conditions (Roberts, 2015).

4.2. Different Crystal Structures Between Sedimentary and Metamorphic Pyrrhotites

Authigenic pyrrhotite from sedimentary nodules (hereafter SPoN) yields a single, intense reflection at a 2θ angle of ~44.03° (Figures 3a–3d), which is distinct from a split, equally intense diffraction doublet at ~43.83° and ~44.05° in metamorphic pyrrhotite (Figure 3f). The characteristic single and double peaks indicate that the sedimentary and metamorphic pyrrhotites have different crystal structures due to hexagonal and monoclinic pyrrhotite, respectively (Arnold, 1966; Graham, 1969). The hexagonal structure of the authigenic pyrrhotite in core MD10-3276 is consistent with the report of van Dongen et al. (2007). Detailed comparison of XRD patterns among different pyrrhotite types, including hexagonal 1 T, 3 T, 4 H, 5 T, 6 T, and 7 T (Figures 3g, 3g-1, and 3g-2), and monoclinic 4 M pyrrhotite (Figures 3f and 3f-1) from the International Centre for Diffraction Data (Mineral Powder Diffraction File Databook, 1993), confirms that the reflections for authigenic sedimentary pyrrhotite in core MD10-3276 best fit the pyrrhotite 3 T type (Figures 3a–3d; Fleet, 1971), whereas metamorphic pyrrhotite extracted from a phyllite is a pyrrhotite 4 M type (Figure 3f; Morimoto et al., 1975).

4.3. Microtextures of Authigenic Minerals in Nodules

SEM observations (Figures 4a–4f) and EDS analyses (Figures 4g–4j) on nodules from core MD10-3276 reveal different microtextural relationships among authigenic iron oxide and sulfide minerals (Figures 3a–3e), which shed light on their diagenetic formation. A nodule from 4.90 m is filled with authigenic crystals (Figure 4a). Voids between crystals are interpreted to be spaces through which methane has passed. Pyrite (S/Fe atomic ratio ≈2.0) and pyrrhotite (S/Fe ratio ≈1.1; Figure 4g) are the two major minerals in the nodule (Figures 4b and 4c), which is consistent with XRD results (Figure 3a). Pyrite occurs with two morphologies: framboidal and nonframboidal, where nonframboidal forms are less common than framboidal pyrite, while pyrrhotite occurs as aggregates of interlocking plates with long dimensions of ~10 μm and thickness of $<$1 μm. The crystal habit of the plates is similar to those reported for authigenic pyrrhotite in other areas, although the dimensions of the plates are variable (Dinarès-Turell & Dekkers, 1999; Kars & Kodama, 2015; Larrasoaña et al., 2007; Roberts, 2015; Rudmin et al., 2018; van Dongen et al., 2007; Weaver et al., 2002). Based on microtextural relationships in Figures 4b and 4c, framboidal pyrite was the first phase to form. Pyrrhotite and nonframboidal pyrite then formed and grew over and around framboidal pyrite. Formation of nonframboidal pyrite after pyrrhotite is inferred because subhedral to euhedral pyrite crystals have grown in the interstices of pyrrhotite aggregates.

Pyrrhotite nodules always have variably oxidized surfaces (Figures 2b–2d). This suggests that the pyrrhotite formed during locally sulfidic/methanic conditions probably associated with methane venting (e.g., Larrasoaña et al., 2007), which was followed by oxic diagenetic conditions during which the iron sulfide nodules underwent variable oxidation. Goethite and minor lepidocrocite appear to be the principal oxidation products (Figures 3c–3e). A diagenetic rather than modern origin is indicated by the fact that goethite crusts are evident on sulfide nodules immediately upon splitting of sealed sediment cores (Figure 2b). Some small nodules are oxidized completely to goethite (Figure 2d) with minor lepidocrocite (Figure 3e). Surficial oxidation is evident in SEM images for nodules from 11.42 and 12.02 m (Figures 3c and 3d), where a goethite crust (Figures 4d and 4h) has grown around the pyrrhotite nodule. In some cases, a goethite-like phase occurs

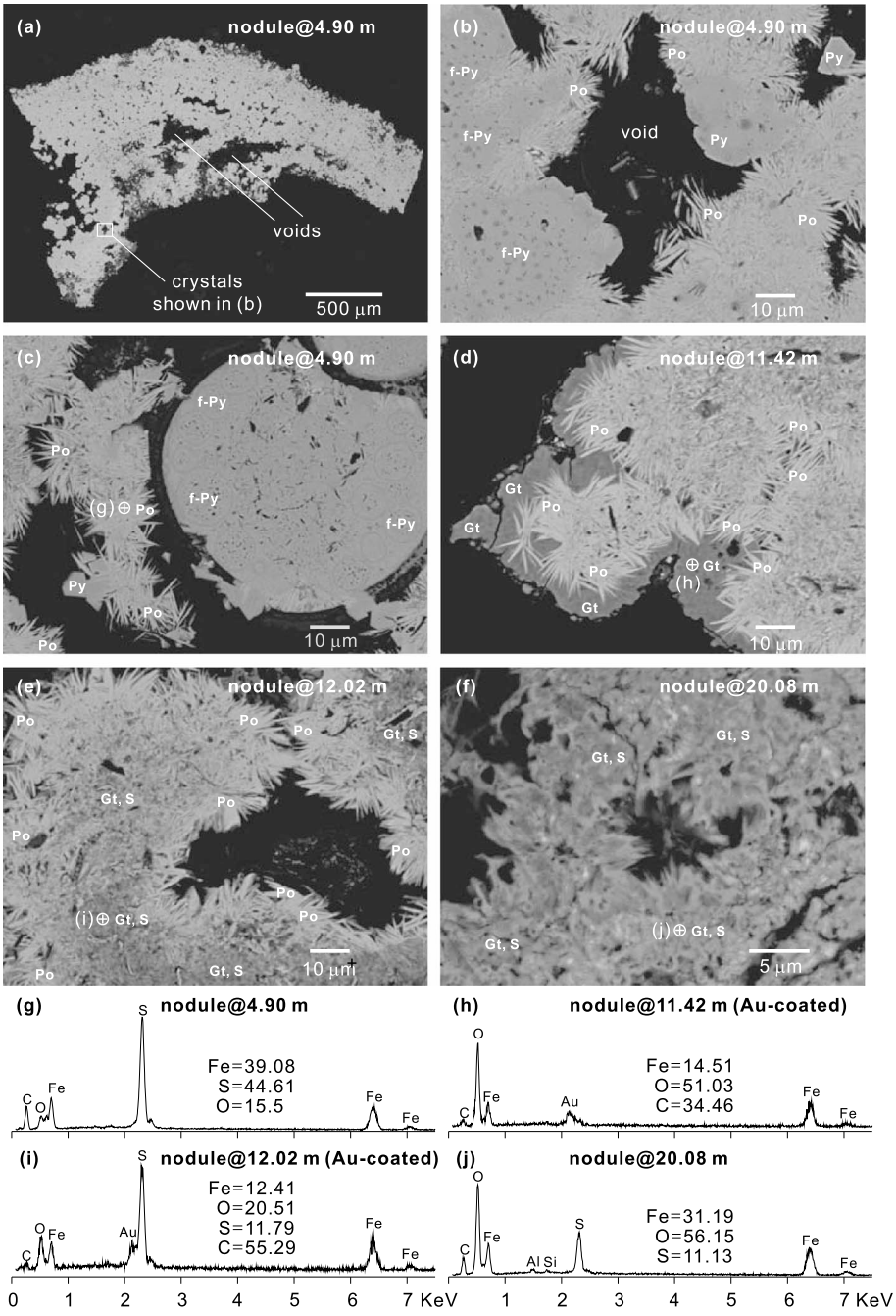

Figure 4. Microscopic characterization of samples analyzed in this study. (a–f) Backscattered scanning electron microscopic images for diagenetic nodules from different depths in core MD10-3276. Py = pyrite in subhedral or euhedral form; f-Py = framboidal pyrite; Po = pyrrhotite; Gt = goethite. Minerals containing S or O have bright or dark contrast, respectively. (g–j) Representative energy dispersive spectrometer results for iron sulfide and oxide minerals in nodules at different depths. The spot positions for analyses are shown with crosses in Figures 4c–4f. The carbon (C) peak detected with energy dispersive spectrometer analysis is produced by the resin that was used to fix the specimens.

within nodules (Figures 4e, 4f, 4i, and 4j), which indicates more pervasive oxidation of nodule interiors. The electron beam used for EDS analysis appears to have interacted simultaneously with pyrrhotite and goethite so that O and S are identified (Figures 4g–4j). The nodule from 20.08 m (Figure 4f) contains more pervasive goethite (Figures 3e, 4f, and 4j), with little S remaining. Overall, textural relationships suggest

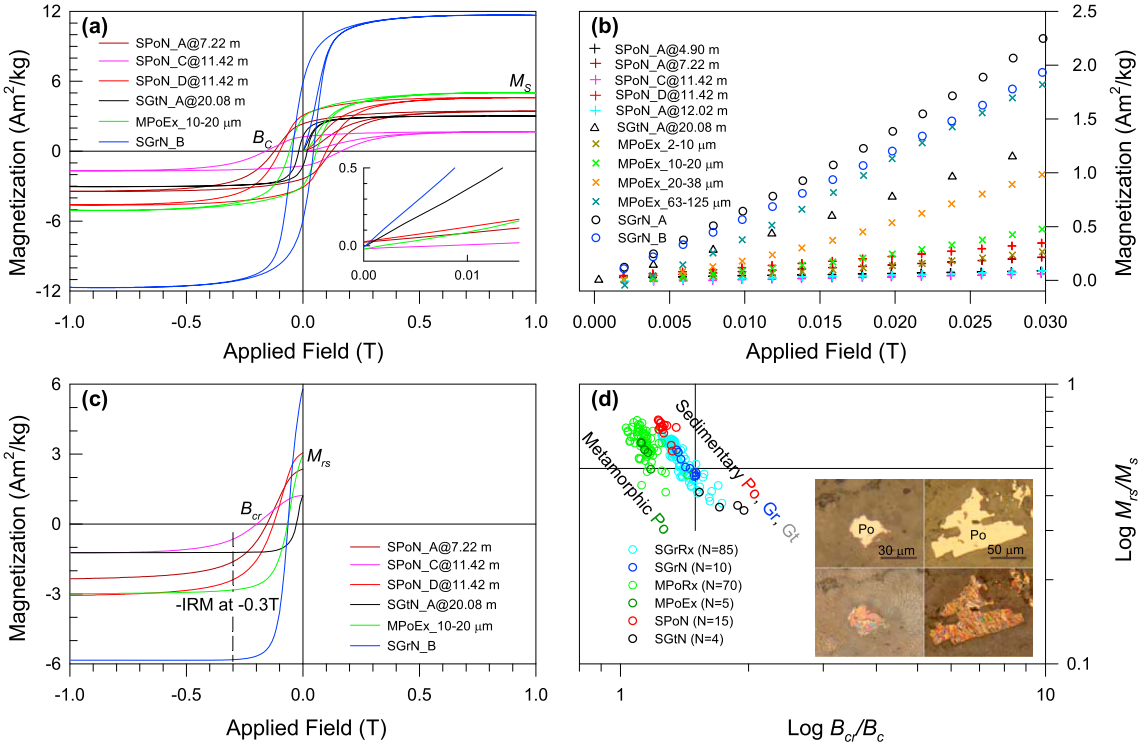

Figure 5. Hysteresis data for samples analyzed in this study. (a) Six representative magnetic hysteresis loops with low-field initial slopes for sedimentary pyrrhotite nodules (SPoN) and sedimentary goethite nodules (SGtN) in core MD10-3276, metamorphic pyrrhotite extracts (MPoEx) with different grain sizes, and sedimentary greigite nodules (SGrN). All loops have been corrected for their high-field slopes. Initial slopes measured at low fields (0–0.015 T) are highlighted in the inset. (b) Initial slope data from additional SPoN, SGtN, MPoEx, and SGrN samples. (c) Backfield demagnetization curves for the six representative samples, which were used to determine S ratios. (d) Bilogarithmic plot of M_{rs}/M_s versus B_{cr}/B_c for all SPoN, SGrN, SGtN, SGrRx, MPoEx, and MPoRx samples subjected to hysteresis analysis (Table 1). Inset: optical images of multidomain magnetic structures in metamorphic pyrrhotite grains observed after smearing polished mineral surfaces with ferrofluid. The upper images are under reflected light; the lower images are for the same polished sections after application of ferrofluid. See text for discussion of the hysteresis values for these multidomain samples.

that goethite formed on nodule surfaces as an oxidation product and that oxidation is pervasive in smaller nodules (Figure 2d) and mainly surficial in larger nodules (Figures 2c and 3).

4.4. Room Temperature Magnetic Properties of Sedimentary and Metamorphic Pyrrhotites, and Sedimentary Greigite

Sedimentary pyrrhotite nodules (SPoN) from core MD10-3276 have distinctive magnetic properties that contrast with those of metamorphic pyrrhotite and sedimentary greigite. Room temperature magnetic properties for the three iron sulfide minerals are illustrated in Figure 5; data for all studied samples are listed in Table 1, including 15 sedimentary pyrrhotite and 4 goethite nodules (SPoN and SGtN, respectively) from core MD10-3276, samples from two land-based (M11 and EJE) sections, including 5 metamorphic pyrrhotite extracts (MPoEx) with variable grain sizes and 10 sedimentary greigite nodules (SGrN). Results for metamorphic pyrrhotite- and greigite-bearing rock samples (MPoRx and SGrRx, N = 70 and 85, respectively) are also summarized in Table 1.

Sedimentary pyrrhotite nodules have high coercivities (B_c >100 mT) and open magnetic hysteresis loops (Table 1 and Figure 5a). In contrast, metamorphic pyrrhotite and sedimentary greigite have relatively narrow loops (Figure 5a) with B_c values ranging from 24 to 71 mT (depending on grain size) and 33 to 57 mT, respectively (Table 1). High B_c values for sedimentary pyrrhotite nodules also make it difficult to reach magnetic saturation. From Figure 5a, applied fields >0.5 T are required for sedimentary pyrrhotite nodules to approach M_s, but M_s is reached at <0.5 T for metamorphic pyrrhotite and sedimentary greigite samples.

Initial slopes of magnetization curves measured at low fields (0–0.03 T) are different for sedimentary and metamorphic pyrrhotite and sedimentary greigite samples (Figures 5a and 5b), which suggests that they

Table 1
Mass-specific Magnetic Parameters (χ, M_{rs}, M_s, B_{cr}, B_c, M_{rs}/M_s, B_{cr}/B_c, and S Ratio) for the Studied Samples, Including Sedimentary Pyrrhotite Nodules (SPoN) and Goethite Nodules (SGtN) From Sediment Core MD10-3276, Metamorphic Pyrrhotite Extracts (MPoEx) With Different Grain Sizes From the M11 Section, and Sedimentary Greigite Nodules (SGrN) From the EJE Section

Sample	Mass (10^{-3}kg)	χ (10^{-6} · m^3/kg)	C_{mm} (%)	M_{rs} (Am^2/kg)	M_s (Am^2/kg)	B_{cr} (mT)	B_c (mT)	M_{rs}/M_s	B_{cr}/B_c	S ratio
SPoN_A@4.90 m	15.7	2.8	83.1	0.730	1.268	144.3	109.0	0.58	1.32	0.71
SPoN_B@4.90 m	60.9	3.2	82.4	0.913	1.511	151.6	115.2	0.60	1.32	0.67
SPoN_A@7.22 m	44.2	8.1	88.6	2.355	3.432	154.6	123.1	0.69	1.26	0.68
SPoN_A@11.42 m	28.2	9.6	90.1	2.942	4.043	162.9	131.3	0.73	1.24	0.65
SPoN_B@11.42 m	27.5	9.6	90.2	2.696	3.709	166.2	133.7	0.73	1.24	0.63
SPoN_C@11.42 m	37.2	3.3	83.8	1.245	1.672	198.5	161.8	0.74	1.23	0.52
SPoN_D@11.42 m	76.1	13.6	91.8	3.074	4.601	126.4	100.0	0.67	1.26	0.78
SPoN_E@11.42 m	21.7	12.7	90.8	3.412	4.952	130.8	106.3	0.69	1.23	0.77
SPoN_F@11.42 m	20.9	6.8	87.6	2.466	3.337	178.1	144.6	0.74	1.23	0.58
SPoN_A@12.02 m	9.9	4.1	86.7	1.148	1.632	152.1	121.2	0.70	1.25	0.66
SPoN_B@12.02 m	25.0	7.4	91.1	1.819	2.588	135.9	109.6	0.70	1.24	0.74
SPoN_C@12.02 m	25.6	5.4	90.0	1.336	1.871	148.8	117.5	0.71	1.27	0.70
SPoN_D@12.02 m	68.6	3.5	88.1	0.765	1.093	159.4	117.9	0.70	1.35	0.59
SPoN_E@12.02 m	40.0	3.8	86.6	0.970	1.385	132.7	106.2	0.70	1.25	0.72
SPoN_F@12.02 m	12.8	4.7	86.3	1.447	2.034	157.4	122.4	0.71	1.29	0.63
SPoN (*N* = 15)								**0.69 ± 0.05**	**1.27 ± 0.04**	
SGtN_A@20.08 m	20.2	53.4	99.0	1.243	3.023	27.8	18.2	0.41	1.53	1.00
SGtN_B@20.08 m	16.6	75.3	99.0	1.888	5.201	33.4	19.6	0.36	1.71	1.00
SGtN_C@20.08 m	17.4	15.6	98.1	0.280	0.761	27.5	14.6	0.37	1.89	1.00
SGtN_D@20.08 m	16.4	8.2	97.0	0.132	0.375	25.3	13.0	0.35	1.95	1.00
SGtN (*N* = 4)								**0.37 ± 0.02**	**1.77 ± 0.16**	
MPoEx_<2 μm	2.3	10.6	89.7	2.921	4.751	79.3	70.8	0.61	1.12	0.96
MPoEx_2-10 μm	10.4	11.7	89.8	2.968	4.791	78.6	70.4	0.62	1.12	0.96
MPoEx_10-20 μm	11.2	21.3	93.4	2.931	5.030	66.2	58.1	0.58	1.14	0.96
MPoEx_20-38 μm	10.1	45.4	96.0	3.900	6.850	56.6	48.8	0.57	1.16	0.98
MPoEx_63-125 μm	12.2	88.1	98.2	3.011	6.070	28.4	24.1	0.50	1.18	1.00
SGrN_A	99.2	95.6	98.6	6.384	12.78	63.2	43.4	0.50	1.46	1.00
SGrN_B	103.8	82.0	98.4	5.902	11.68	64.3	45.2	0.51	1.42	1.00
SGrN_C	69.5	94.4	98.6	5.757	12.22	60.6	40.3	0.47	1.50	1.00
SGrN_D	23.0	89.6	98.3	7.533	13.98	71.2	51.3	0.54	1.39	1.00
SGrN_E	82.0	192.8	99.1	9.095	19.45	54.6	36.6	0.47	1.49	1.00
SGrN_F	107.1	61.0	98.5	3.279	6.79	60.7	40.3	0.48	1.50	0.99
SGrN_G	89.6	105.4	99.2	4.318	9.18	49.3	32.9	0.47	1.50	0.99
SGrN_H	82.4	119.2	98.9	6.164	12.79	57.3	38.5	0.48	1.49	0.99
SGrN_I	95.2	60.5	98.1	4.970	8.54	73.8	54.4	0.58	1.35	0.98
SGrN_J	125.1	74.2	98.1	6.385	11.18	77.9	57.0	0.57	1.37	0.98
SGrN (*N* = 10)								**0.51 ± 0.04**	**1.45 ± 0.06**	
SGrRx (*N* = 85)								**0.55 ± 0.08**	**1.38 ± 0.10**	
MPoRx (*N* = 70)								**0.61 ± 0.07**	**1.14 ± 0.06**	

Note. Only means and standard deviations (bold) of M_{rs}/M_s and B_{cr}/B_c are listed for metamorphic pyrrhotite-bearing rocks (MPoRx) and sedimentary greigite-bearing rocks (SGrRx). Approximate concentrations of magnetic minerals (C_{mm}) in the studied samples were estimated using the ratio of the corrected low-field slope of hysteresis loops to the noncorrected slope (see the supporting information for procedures).

have different low-field mass-specific magnetic susceptibilities (χ). To illustrate this relationship, initial slope data after correction for high-field slopes and divided by specimen mass (i.e., which gives χ) are replotted in Figure 5a (inset) with data for additional samples in Figure 5b. The χ values obtained from this procedure (see the supporting information for details) are listed in Table 1. The χ values for sedimentary pyrrhotite nodules, which contain variable pyrite, S, goethite, and quartz contents (Figures 3a–3d), fall in the 2–14 × 10^{-6} m^3/kg range. Regardless of these impurities, χ values for sedimentary pyrrhotite nodules are slightly lower than or close to those of finer-grained (<10 μm) metamorphic pyrrhotite (i.e., 11–12 × 10^{-6} m^3/kg; see Table 1 and Figure 5b) but are much lower than those of coarser-grained (>10 μm) metamorphic pyrrhotite (21–88 × 10^{-6} m^3/kg) and sedimentary greigite nodules (60–193 × 10^{-6} m^3/kg).

The high coercivities of sedimentary pyrrhotite nodules also result in low S ratios determined from backfield demagnetization curves (Figure 5c). Sedimentary pyrrhotite nodules have S ratios that range from 0.52 to

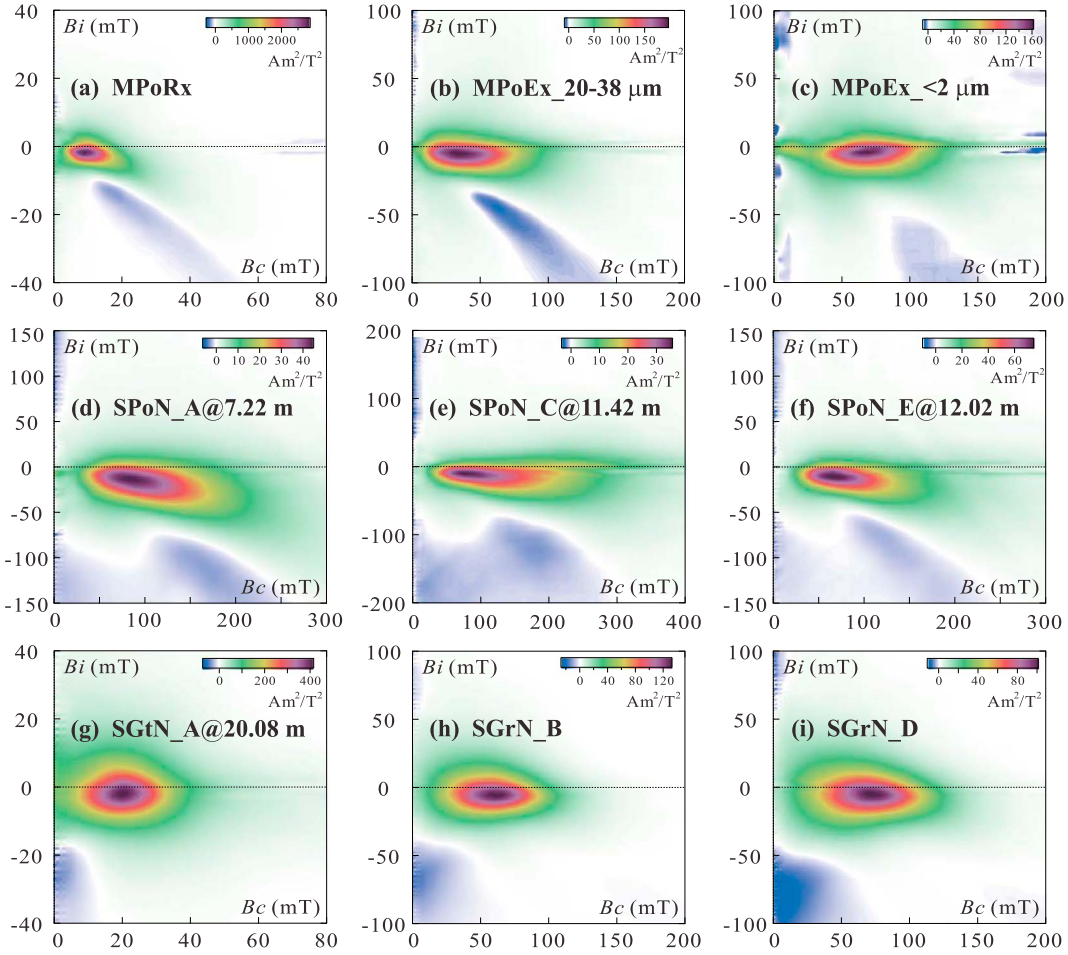

Figure 6. First-order reversal curve (FORC) diagrams for samples studied here. FORC diagrams are shown for (a) monoclinic pyrrhotite from bulk metamorphic rocks (MPoRx), (b) monoclinic pyrrhotite extracted from metamorphic rocks and sieved to the 20–38 μm size fraction (MPoEx_20–38 μm), and (c) the <2 μm fraction (MPoEx_ <2 μm); authigenic pyrrhotite nodules (d) SPoN_A@7.22 m, (e) SPoN_C@11.42 m, and (f) SPoN_E@12.02 m; (g) a goethite nodule (SGtN_A@20.08 m), and greigite from sedimentary nodules (h) SGrN_B and (i) SGrN_D. VARIFORC parameters (Egli, 2013) used to smooth the FORC diagrams are as follows: $s_{c,0} = 4$, $s_{c,1} = 7$, $s_{b,0} = 3$, $s_{b,1} = 7$, and $\lambda_c = \lambda_b = 0.1$.

0.78 (Table 1), which are much lower than for metamorphic pyrrhotite (0.96–1.00) and greigite nodules (0.98–1.00). Low S ratios down to ~0.7 are also observed in authigenic pyrrhotite-bearing sediments from Nankai Trough, offshore of Japan (Kars & Kodama, 2015).

Hysteresis parameter ratios for sedimentary pyrrhotite nodules are 0.58–0.74 for M_{rs}/M_s and 1.23–1.35 for B_{cr}/B_{c}, which are slightly larger than for metamorphic pyrrhotite (Table 1). Despite the small difference between them, the two pyrrhotite types yield different trends on a bilogarithmic M_{rs}/M_s versus B_{cr}/B_c plot (Figure 5d). Data for sedimentary pyrrhotite lie along the same trend as sedimentary greigite data. In contrast, data for metamorphic pyrrhotite lie along another trend located to the left of the sedimentary greigite-pyrrhotite trend. These results are suggested to be due to different crystal and magnetic domain structures in the metamorphic and sedimentary pyrrhotites, where the former is monoclinic (Figure 3f) with large (multi-domain, MD) grain sizes (Figure 5d inset).

FORC diagrams (Figure 6) also indicate that different magnetic properties exist among the studied metamorphic and sedimentary pyrrhotite, and goethite and greigite samples. All pyrrhotite samples, regardless of their metamorphic or sedimentary origins (Figures 6a–6f), have kidney-shaped FORC distributions with negative slopes, as have been reported before for pyrrhotite (Larrasoaña et al., 2007; Roberts et al., 2006, 2010, 2014; Weaver et al., 2002; Wehland et al., 2005), that lie largely below the $B_i = 0$ axis. The sedimentary

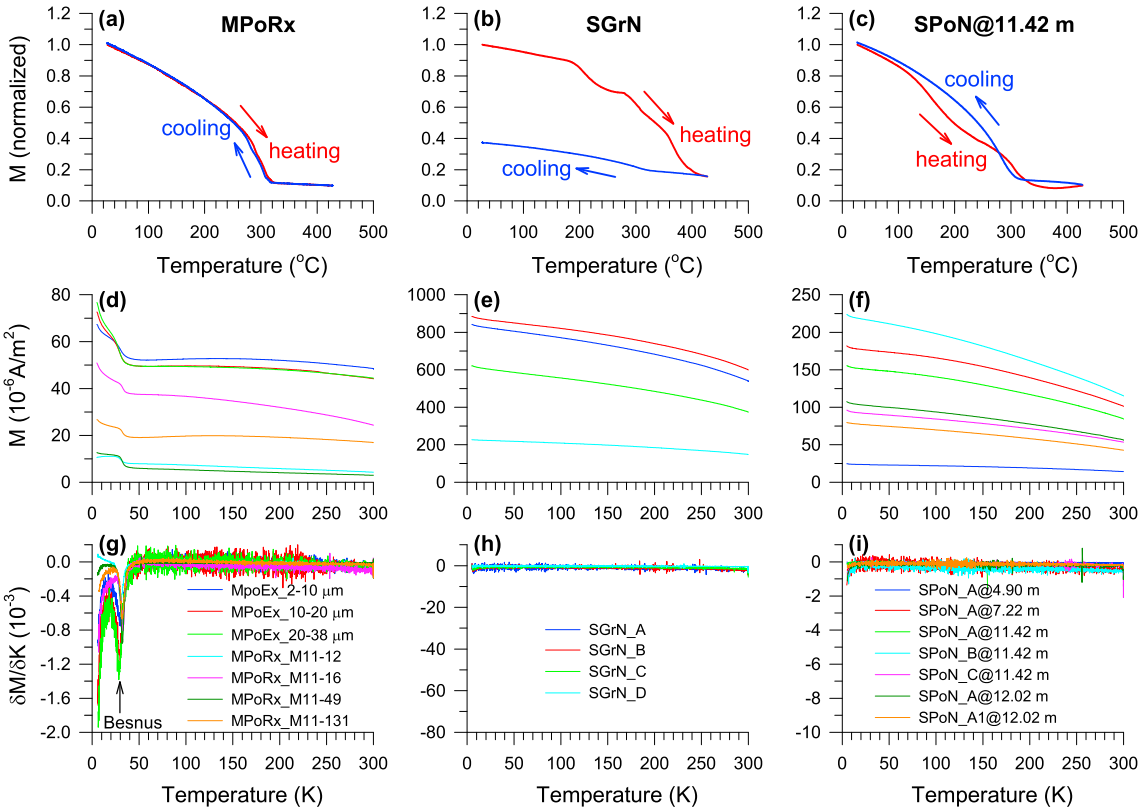

Figure 7. High- and low-temperature magnetic results for the three types of studied iron sulfide samples. (a–c) Thermomagnetic curves for MPoRx, SGrN, and SPoN samples (heated under vacuum at 3 T) measured to 427°C. (d–f) Low-temperature (5–300-K) saturation isothermal remanent magnetization (5-T) warming curves for sieved MPoEx with different sizes, and for MPoRx, SGrN, and SPoN samples. (g–i) First derivatives (δM/δK) of the saturation isothermal remanent magnetization curves with respect to temperature are plotted for the data shown in (d–f) to highlight the presence of possible magnetic transitions during warming. Only the Besnus transition at ~34 K is recognized for metamorphic pyrrhotite (MPoEx and MPoRx) samples.

pyrrhotite samples (Figures 6d–6f) have higher coercivities than the metamorphic pyrrhotites (Figures 6a–6c). The goethite nodule (Figure 6g) has relatively low coercivities that are consistent with the respective magnetic hysteresis loop (Figure 5a and Table 1) but with much lower coercivities than expected for stable single domain (SD) goethite (Roberts et al., 2006). FORC diagrams for greigite nodules (Figures 6h and 6i) are more symmetric than those for pyrrhotite samples, and are indicative of strong magnetostatic interactions and moderate coercivities, as has been documented extensively (Florindo et al., 2007; Larrasoaña et al., 2007; Roberts et al., 2000, 2006, 2011; Vasiliev et al., 2007).

4.5. High- and Low-Temperature Magnetic Characteristics of Sedimentary and Metamorphic Pyrrhotites, and Sedimentary Greigite

Metamorphic pyrrhotite has reversible heating and cooling curves with a Curie temperature of 318 ± 2°C (Figure 7a), which coincides with the expected value of 320°C (Dekkers, 1989). Sedimentary greigite and pyrrhotite have irreversible curves due to thermal alteration and iron mineral neoformation (Figures 7b and 7c), which indicates that they are less stable than metamorphic pyrrhotite during heating.

Pyrrhotite and greigite have contrasting magnetic characteristics at low temperatures. Pyrrhotite clearly exhibits the Besnus magnetic transition at ~34 K in low-temperature SIRM warming curves, whereas greigite lacks a transition (Besnus & Meyer, 1964; Chang et al., 2009; Dekkers et al., 1989; Fillion & Rochette, 1988; Moskowitz et al., 1993; Roberts, 1995; Roberts et al., 2010; Rochette et al., 1990; Torii et al., 1996). The metamorphic pyrrhotite and sedimentary greigite samples studied here behave as expected with a Besnus transition and no transition, respectively (Figures 7d, 7e, 7g, and 7h). Metamorphic pyrrhotite has a Besnus transition regardless of its grain size for the studied size range (Figure 7g). In contrast, sedimentary pyrrhotite nodules have similar behavior to greigite with no magnetic transition detected (Figures 7f and 7i).

5. Discussion

5.1. Magnetism in Hexagonal Pyrrhotite?

Monoclinic pyrrhotite is ferrimagnetic, whereas hexagonal pyrrhotite (Fe_9S_{10} or $Fe_{11}S_{12}$) is antiferromagnetic (O'Reilly et al., 2000), so it should not carry a remanent magnetization at room temperature. Thus, when magnetic pyrrhotite is found in sediments, it has been assumed routinely to be monoclinic (e.g., Kars & Kodama, 2015; Larrasoaña et al., 2007; Roberts, 2015; Weaver et al., 2002). The crystal structure of sedimentary pyrrhotite has not been investigated widely to assess this assumption.

In this study, the single intense reflection at ~44.03° observed from synchrotron XRD results for sedimentary pyrrhotite nodules is due only to hexagonal (3 T) pyrrhotite (Figures 3a–3d). The studied sedimentary pyrrhotite nodules are moderately magnetic, with weaker magnetizations than sedimentary greigite and coarse metamorphic pyrrhotite, and similar magnetizations to fine metamorphic pyrrhotite (Figure 5b). The biggest difference in magnetic properties among the studied iron sulfides is that the sedimentary pyrrhotite nodules (Figures 6d–6f) have higher coercivities than the studied greigite (Figures 6h and 6i) and monoclinic pyrrhotite (Figures 6a–6c), although fine-grained metamorphic pyrrhotite can also have similarly high coercivities (Clark, 1984; Dekkers, 1988), especially those measured by Clark (1984).

In assessing the origin of the observed magnetization of the sedimentary hexagonal pyrrhotite nodules, which are readily attracted magnetically by a rare earth magnet, it is important to determine whether known magnetic minerals could be responsible for the magnetic signal. Synchrotron XRD results enable detection of minerals with concentrations $<0.1\%$; the only other magnetic mineral identified in Figures 3a–3d is goethite. Goethite has extraordinarily high coercivities and is not saturated even at 57 T (e.g., Rochette et al., 2005). The possibility that goethite could be responsible for the high coercivities observed in the sedimentary pyrrhotite nodules was tested by magnetic analysis of a goethite nodule from a depth of 20.08 m in core MD10-3276. This nodule (sample SGtN_A) contains no pyrrhotite (Figure 3e) and has low coercivity (Figure 5a). The low coercivity of the goethite-dominated nodule may be surprising and requires explanation. The goethite observed by XRD and under SEM is at least partially crystalline (Figures 3c–3e and 4d–4f). The fact that goethite requires high fields to saturate magnetically means that this crystalline goethite may not be magnetized significantly in the maximum applied field of 1 T used in this study. In contrast, finer nanogoethite particles occur commonly in natural environments and have no remanence or coercivity (Till et al., 2015; van der Zee et al., 2003). A combination of high-coercivity goethite with nanogoethite could, therefore, explain the observed low coercivity of goethite nodule SGtN_A. Importantly, the low coercivity of goethite nodules cannot explain the high coercivity of the studied sedimentary pyrrhotite nodules. The goethite nodule also contains traces of greigite (Figure 3e), which has lower coercivity than the studied sedimentary pyrrhotite nodules (Figure 5a), and lepidocrocite (Figure 3e), which is not magnetic at room temperature. Thus, neither of these minerals can explain the magnetic properties observed for the sedimentary pyrrhotite nodules. Magnetite is not detected in XRD analyses, and even small traces of magnetite will be evident in low-temperature magnetization results (Chang et al., 2016), so it can be excluded as a low-concentration contaminant in the studied samples. XRD results (Figures 3a–3d) fail to identify a potential contaminant that can explain the magnetic properties of the studied hexagonal pyrrhotite nodules and magnetic results (Figure 5) fail to explain the high observed coercivities of these samples from the range of potential contaminants considered.

It is not yet possible to explain the magnetization observed in the studied sedimentary pyrrhotite nodules. The pyrrhotite family of minerals has variable Fe/S ratios, with various distributions of Fe site vacancies that produce either ferrimagnetic or antiferromagnetic superstructures (Pósfai et al., 2000). Many superstructures can exist with the same crystallographic *c* dimension and Fe/S ratio (Pósfai & Dódony, 1990). XRD data obtained here indicate a hexagonal 3 T pyrrhotite type with insufficient contamination from other magnetic minerals to explain the observed magnetic properties. It is, therefore, proposed tentatively here that the hexagonal pyrrhotite in the studied sedimentary pyrrhotite nodules has intrinsic magnetic properties with moderate magnetization and high coercivity. It may be that the magnetization is due to a previously unrecognized magnetism in hexagonal (3 T) pyrrhotite. Confirmation of a room temperature magnetization in hexagonal (3 T) pyrrhotite awaits neutron diffraction or Mössbauer analysis to determine the sublattice magnetizations to understand any potential deviation from the expected antiferromagnetic structure in hexagonal pyrrhotite. Future detailed work of this type is beyond the scope of the present study but is planned to enable more complete explanation of the hypothesized magnetism in hexagonal pyrrhotite.

It is possible that a lamellar-type magnetization such as that proposed by Robinson et al. (2002) could give rise to magnetism in the studied hexagonal (3 T) pyrrhotite due to stacking of ferrimagnetically and antiferromagnetically coupled superstructures (e.g., Powell et al., 2004; Wang & Salveson, 2005) perpendicular to the basal plane of pyrrhotite. Lamellar magnetizations have been proposed to result from ferrous-ferric contact layers that reduce charge imbalance along lamellar contacts between canted antiferromagnetic hematite and paramagnetic ilmenite intergrowths to produce strong M_s and high coercivity (Robinson et al., 2002). Such a possibility is tested readily for pyrrhotite because lamellar magnetizations are characterized by shifted negatively low-temperature hysteresis loops due to strong exchange bias associated with exchange coupling across hematite-ilmenite interfaces (Fabian et al., 2008). The low-temperature magnetic properties of authigenic and monoclinic pyrrhotite are discussed in detail by Horng and Roberts (2018), who demonstrate that low-temperature hysteresis loops are symmetrical and lack the large negative shifts observed by Fabian et al. (2008) in association with lamellar magnetizations. Thus, a lamellar-type magnetization can be ruled out as a cause of the room temperature magnetization in hexagonal (3 T) pyrrhotite.

For the purposes of sedimentary magnetic investigations, an important conclusion from this study is that identification of magnetic pyrrhotite in sediments should not lead to the automatic conclusion that the pyrrhotite is monoclinic. Care is, therefore, needed to distinguish between monoclinic and hexagonal pyrrhotite in sediments. XRD or electron microscope analyses can provide the necessary complementary constraints for such interpretations.

5.2. Low-Temperature Magnetic Properties of Magnetic Iron Sulfide Minerals

The results shown in Figure 7 demonstrate that the Besnus transition at ~34 K (Besnus & Meyer, 1964; Dekkers et al., 1989; Fillion & Rochette, 1988; Rochette et al., 1990) is observed only for monoclinic pyrrhotite. Hexagonal pyrrhotite demonstrably lacks a low-temperature magnetic transition, as does greigite (Chang et al., 2009; Moskowitz et al., 1993; Roberts, 1995; Roberts et al., 2010; Torii et al., 1996). Lack of a Besnus transition in hexagonal pyrrhotite provides one way of avoiding confusion with monoclinic pyrrhotite, but lack of a phenomenon is not a diagnostic property. The clearest way to discriminate between hexagonal and monoclinic pyrrhotite is to undertake XRD or electron microscope analyses.

Weaver et al. (2002) and Kars and Kodama (2015) suggested that sedimentary pyrrhotite gives rise to a Besnus transition signature in gas hydrate-bearing sediments in Sakhalin, Russia, and Nankai Trough, offshore of Japan, respectively. The magnetization change at 30–40 K noted by Weaver et al. (2002) was not observed clearly, and they did not provide a confident interpretation of this feature. Kars and Kodama (2015) observed a clear inflection in low-temperature magnetization data at 30–40 K. Based on the results presented here, the inflections observed in either study will not be due to authigenic pyrrhotite. If they represent a genuine Besnus transition signature, the signature is more likely to be due to detrital monoclinic pyrrhotite that eroded from various igneous or metamorphic sources in nearby onshore regions. Alternatively, the magnetization change at 30–40 K could be due to siderite (Frederichs et al., 2003; Housen et al., 1996), which is a common authigenic mineral in methanic sediments (Larrasoaña et al., 2007; Roberts, 2015), or to rhodochrosite (Frederichs et al., 2003; Kosterov et al., 2006), which is less likely in such environments. Care should be taken to assess such ambiguities in sediment magnetic studies, particularly in gas hydrate-bearing and methanic sediments.

5.3. Contrasting Magnetic Properties of Magnetic Iron Sulfide Minerals

The main finding of this study is that sedimentary magnetic iron sulfide minerals have contrasting magnetic properties (Figures 5 and 6). Hexagonal (3 T) pyrrhotite appears to be capable of carrying a room temperature magnetization rather than being antiferromagnetic, but it does not have a low-temperature magnetic transition. The Besnus transition is only observed in monoclinic pyrrhotite (Figure 7). Thus, the assumption that monoclinic pyrrhotite is responsible for magnetic signals when magnetic pyrrhotite is encountered in sedimentary environments seems to be incorrect. The inference from this study that hexagonal pyrrhotite can carry a room temperature magnetization needs to be verified by assessment of the sublattice magnetizations from neutron diffraction or Mössbauer analysis, but the present results provide a significant basis for concluding that hexagonal and monoclinic pyrrhotite both carry room temperature magnetizations that contrast with each other. Furthermore, the magnetic properties of hexagonal and monoclinic pyrrhotite contrast with those of sedimentary greigite.

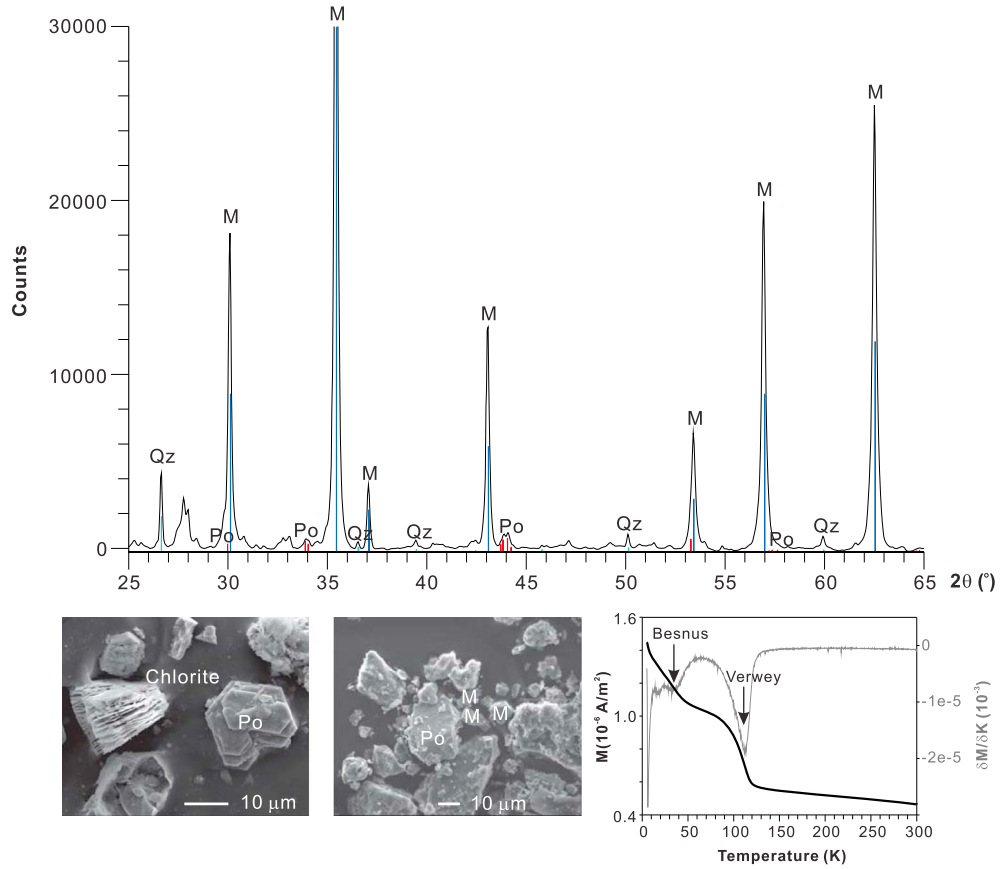

Figure 8. Illustration of the magnetic identification of mixed magnetic minerals in sediments. From X-ray diffraction data (above), magnetite (M) is the dominant mineral identified in a magnetic extract from bulk sediments with grain sizes <63 μm from a depth of 11.42 m in core MD10-3276. Minor monoclinic pyrrhotite (Po) and quartz (Qz) are also evident. In the two secondary electron scanning electron microscope images on the lower left-hand side of the figure, detrital pyrrhotite and magnetite are identified (along with chlorite). In low-temperature magnetization data, a strong Verwey transition signal due to magnetite is evident at 110–120 K with a weaker Besnus transition signal at ~34 K (lower right-hand side).

Key magnetic properties for the three studied magnetic iron sulfide minerals are as follows. Monoclinic pyrrhotite has relatively weak to moderate magnetizations (Figure 5b), similar coercivities to greigite (Figures 5a and 5c), similar M_{rs}/M_s values to greigite and hexagonal pyrrhotite, but lower respective B_{cr}/B_c values (Figure 5d). This difference in B_{cr}/B_c values distinguishes the metamorphic monoclinic pyrrhotite samples from sedimentary greigite and hexagonal pyrrhotite. Neither greigite nor hexagonal pyrrhotite has a low-temperature magnetic transition. Hexagonal pyrrhotite has high coercivity (Figures 5a and 5c) and relatively weak magnetizations (Figure 5b), whereas greigite has strong magnetization and intermediate coercivity. The documented magnetic properties should prove useful in discriminating sedimentary magnetic iron sulfides from each other, particularly when coupled with diagnostic mineralogical identifications from XRD analysis and SEM observations.

It is important to note that although the metamorphic monoclinic pyrrhotite samples generally have M_{rs}/M_s values >0.5 and B_{cr}/B_c values <1.2 (Table 1), these values are not necessarily indicative of SD properties. Complex domain structures are evident in the large particles illustrated in Figure 5d (30 μm and larger) when their polished surfaces are smeared with ferrofluid. Monoclinic pyrrhotite has multiaxial rather than uniaxial anisotropy (Martín-Hernández et al., 2008), for which theoretical SD values are $M_{rs}/M_s = 0.75$ (Dunlop, 1971) rather than $M_{rs}/M_s = 0.5$ for uniaxial SD particles (Stoner & Wohlfarth, 1948). Like pyrrhotite, hematite has multiaxial anisotropy with magnetization in the crystallographic basal plane. The descending branch of hysteresis loops for MD hematite decreases slowly from saturation to yield M_{rs}/M_s values >0.5 (Özdemir & Dunlop,

2014). Similarly high M_{rs}/M_s values for pyrrhotite are, likewise, not necessarily indicative of the dominance of SD particles. Nevertheless, FORC diagrams for these samples (Figure 6) contain concentric contours that are indicative of SD particles, although the observed magnetic properties are not due only to SD particles; rather, the evidence indicates that samples with coarse monoclinic pyrrhotite particles contain mixtures of particles in the SD, vortex, and MD states. Measurements of transient contributions to FORCs (Zhao et al., 2017) would enable separation of SD, vortex, and MD contributions to the total magnetization of these pyrrhotite samples, which is beyond the scope of the present study. Such analyses are planned for the future.

5.4. Discrimination of Magnetic Iron Sulfides in Sediments

Based on the above, it is possible to illustrate the discrimination of sedimentary magnetic iron sulfides from mineralogical and magnetic analyses (Figure 8). A magnetic extract from nodule-bearing host sediment ($<$63 μm) at a depth of 11.42 m in core MD10-3276 is dominated by magnetite, as is evident in XRD results; it also contains minor monoclinic pyrrhotite with a clear double peak at 2θ angles of ~43.83° and ~44.05°. Both magnetite and monoclinic pyrrhotite are evident in SEM images and in low-temperature magnetic measurements where a strong Verwey transition is apparent at 110–120 K, which is indicative of detrital rather than biogenic magnetite (Chang et al., 2016), and a Besnus transition due to monoclinic pyrrhotite is apparent at ~34 K (Figure 8), which is also indicative of a detrital origin. The approach illustrated here has considerable scope for assisting interpretation of sedimentary magnetic records.

6. Conclusions

It is demonstrated here that three relatively abundant magnetic iron sulfide minerals, hexagonal and monoclinic pyrrhotite and greigite, have contrasting magnetic properties, which coupled with mineralogical characterizations, enables interpretation of the paleomagnetic and environmental signals that they carry. Such differentiation is critical to recognizing their potentially contrasting origins (i.e., diagenetic versus detrital). The results presented here should have wide applicability in sedimentary magnetic studies.

Acknowledgments

The author is grateful to Kuo-Hang Chen and Chun-Hung Lin for their assistance in laboratory work, the National Synchrotron Radiation Research Center, Taiwan, for XRD analyses, Andrew Roberts for helpful discussions, and the journal reviewers (Myriam Kars and anonymous) and Editors (Mark Dekkers and Michael Walter) for comments that helped to improve the manuscript. This work was supported financially by the Central Geological Survey and the Ministry of Science and Technology, Taiwan, through grant 104-5226904000-02-01 and MOST 105-2116-M-001-018. Data presented in this paper are available at http://dmc.earth.sinica.edu.tw/Contributor/Horng/2018mag/.

References

Arnold, R. G. (1966). Mixtures of hexagonal and monoclinic pyrrhotite and the measurement of the metal content of pyrrhotite by X-ray diffraction. *American Mineralogist*, *51*, 1221–1227.

Besnus, M. J., & Meyer, A. J. (1964). *Nouvelles données expérimentales sur le magnétisme de la pyrrhotine naturelle*. Paper presented at Proceedings of the International Conference on Magnetism, Nottingham, England (pp. 507–511).

Chang, L., Heslop, D., Roberts, A. P., Rey, D., & Mohamed, K. J. (2016). Discrimination of biogenic and detrital magnetite through a double Verwey transition temperature. *Journal of Geophysical Research: Solid Earth*, *121*, 3–14. https://doi.org/10.1002/2015JB012485

Chang, L., Roberts, A. P., Rowan, C. J., Tang, Y., Pruner, P., Chen, Q., & Horng, C.-S. (2009). Low-temperature magnetic properties of greigite (Fe_3S_4). *Geochemistry, Geophysics, Geosystems*, *10*, Q01Y04. https://doi.org/10.1029/2008GC002276

Chen, S.-C., Hsu, S.-K., Wang, Y., Chung, S.-H., Chen, P.-C., Tsai, C.-H., et al. (2014). Distribution and characters of the mud diapirs and mud volcanoes off southwest Taiwan. *Journal of Asian Earth Sciences*, *92*, 201–214. https://doi.org/10.1016/j.jseaes.2013.10.009

Chiu, J.-K., Tseng, W.-H., & Liu, C.-S. (2006). Distribution of gassy sediments and mud volcanoes offshore southwestern Taiwan. *Terrestrial, Atmospheric and Oceanic Sciences*, *17*, 703–722. https://doi.org/10.3319/TAO.2006.17.4.703(GH)

Chuang, P.-C., Yang, T. F., Lin, S., Lee, H.-F., Lan, T. F., Hong, W.-L., et al. (2006). Extremely high methane concentration in bottom water and cored sediments from offshore southwestern Taiwan. *Terrestrial, Atmospheric and Oceanic Sciences*, *17*, 903–920. https://doi.org/10.3319/TAO.2006.17.4.903(GH)

Clark, D. A. (1984). Hysteresis properties of sized dispersed monoclinic pyrrhotite grains. *Geophysical Research Letters*, *11*, 173–176. https://doi.org/10.1029/GL011i003p00173

Dekkers, M. J. (1988). Magnetic properties of natural pyrrhotite. Part I. Behaviour of initial susceptibility and saturation-magnetization-related rock-magnetic parameters in a grain-size dependent framework. *Physics of the Earth and Planetary Interiors*, *52*, 376–393. https://doi.org/10.1016/0031-9201(88)90129-X

Dekkers, M. J. (1989). Magnetic properties of natural pyrrhotite. II. High- and low-temperature behaviour of *Jrs* and TRM as function of grain size. *Physics of the Earth and Planetary Interiors*, *57*, 266–283. https://doi.org/10.1016/0031-9201(89)90116-7

Dekkers, M. J., Mattéi, J.-L., Fillion, G., & Rochette, P. (1989). Grain-size dependence of magnetic behavior of pyrrhotite during its low temperature transition at 34 K. *Geophysical Research Letters*, *16*, 855–858. https://doi.org/10.1029/GL016i008p00855

Dinarès-Turell, J., & Dekkers, M. J. (1999). Diagenesis and remanence acquisition in the Lower Pliocene Trubi marls at Punta di Maiata (southern Sicily): Paleomagnetic and rock magnetic observations. In D. H. Tarling, & P. Turner (Eds.), *Palaeomagnetism and diagenesis in sediments*. *Geological Society of London, Special Publication, 151*, 53–69.

Dunlop, D. J. (1971). Magnetic properties of fine particle hematite. *Annales de Géophysique*, *27*, 269–293.

Egli, R. (2013). VARIFORC: An optimized protocol for calculating non-regular first-order reversal curve (FORC) diagrams. *Global and Planetary Change*, *110*, 302–320.

Fabian, K., McEnroe, S. A., Robinson, P., & Shcherbakov, V. P. (2008). Exchange bias identifies lamellar magnetism as the origin of the natural remanent magnetization in titanohematite with ilmenite exsolution from Modum, Norway. *Earth and Planetary Science Letters*, *268*, 339–353.

Fillion, G., & Rochette, P. (1988). The low temperature transition in monoclinic pyrrhotite. *Journal de Physique, Colloques*, *49*, C8-907–C8-908. https://doi.org/10.1051/jphyscol:19888412

Fleet, M. E. (1971). The crystal structure of a pyrrhotite (Fe_7S_8). *Acta Crystallographica*, *B27*, 1864–1867. https://doi.org/10.1107/S0567740871004990

Florindo, F., Karner, D. B., Marra, F., Renne, P. R., Roberts, A. P., & Weaver, R. (2007). Radioisotopic age constraints for Glacial Terminations IX and VII from aggradational sections of the Tiber River delta in Rome, Italy. *Earth and Planetary Science Letters*, *256*, 61–80.

Frederichs, T., von Dobeneck, T., Bleil, U., & Dekkers, M. (2003). Towards the identification of siderite, rhodochrosite, and vivianite in sediments by their low-temperature magnetic properties. *Physics and Chemistry of the Earth*, *28*, 669–679. https://doi.org/10.1016/S1474-7065(03)00121-9

Graham, A. R. (1969). Quantitative determination of hexagonal and monoclinic pyrrhotites by X-ray diffraction. *Canadian Mineralogist*, *10*, 4–24.

Harrison, R. J., & Feinberg, J. M. (2008). FORCinel: An improved algorithm for calculating first-order reversal curve distributions using locally weighted regression smoothing. *Geochemistry, Geophysics, Geosystems*, *9*, Q05016. https://doi.org/10.1029/2008GC001987

Horng, C.-S., & Chen, K.-H. (2006). Complicated magnetic mineral assemblages in marine sediments offshore southwestern Taiwan: Possible influences of methane flux on the early diagenetic process. *Terrestrial, Atmospheric and Oceanic Sciences*, *17*, 1009–1026. https://doi.org/10.3319/TAO.2006.17.4.1009(GH)

Horng, C.-S., & Huh, C.-A. (2011). Magnetic properties as tracers for source-to-sink dispersal of sediments: A case study in the Taiwan Strait. *Earth and Planetary Science Letters*, *309*, 141–152. https://doi.org/10.1016/j.epsl.2011.07.002

Horng, C.-S., Huh, C.-A., Chen, K.-H., Lin, C.-H., Shea, K.-S., & Hsiung, K.-H. (2012). Pyrrhotite as a tracer for denudation of the Taiwan orogen. *Geochemistry, Geophysics, Geosystems*, *13*, Q08Z47. https://doi.org/10.1029/2012GC004195

Horng, C.-S., & Roberts, A. P. (2006). Authigenic or detrital origin of pyrrhotite in sediments?: Resolving a paleomagnetic conundrum. *Earth and Planetary Science Letters*, *241*, 750–762. https://doi.org/10.1016/j.epsl.2005.11.008

Horng, C.-S., & Roberts, A. P. (2018). The low-temperature Besnus magnetic transition: Signals due to monoclinic and hexagonal pyrrhotite. *Geochemistry, Geophysics, Geosystems*, *19*. https://doi.org/10.1029/2017GC007394

Housen, B. A., Banerjee, S. K., & Moskowitz, B. M. (1996). Low temperature magnetic properties of siderite and magnetite in marine sediments. *Geophysical Research Letters*, *23*, 2843–2846. https://doi.org/10.1029/96GL01197

Jiang, W.-T., Horng, C.-S., Roberts, A. P., & Peacor, D. R. (2001). Contradictory magnetic polarities in sediments and variable timing of neoformation of authigenic greigite. *Earth and Planetary Science Letters*, *193*, 1–12. https://doi.org/10.1016/S0012-821X(01)00497-6

Kars, M., & Kodama, K. (2015). Authigenesis of magnetic minerals in gas hydrate-bearing sediments in the Nankai Trough, offshore Japan. *Geochemistry, Geophysics, Geosystems*, *16*, 947–961. https://doi.org/10.1002/2014GC005614

King, J. W., & Channell, J. E. T. (1991). Sedimentary magnetism, environmental magnetism, and magnetostratigraphy. U.S. National Report to International Union of Geodesy and Geophysics 1987-1990. *Reviews of Geophysics*, *29*, 358–370. https://doi.org/10.1002/rog.1991.29.s1.358

Kosterov, A., Frederichs, T., & von Dobeneck, T. (2006). Low-temperature magnetic properties of rhodochrosite ($MnCO_3$). *Physics of the Earth and Planetary Interiors*, *154*, 234–242. https://doi.org/10.1016/j.pepi.2005.09.011

Larrasoaña, J. C., Roberts, A. P., Musgrave, R. J., Gràcia, E., Piñero, E., Vega, M., & Martínez-Ruiz, F. (2007). Diagenetic formation of greigite and pyrrhotite in gas hydrate marine sedimentary systems. *Earth and Planetary Science Letters*, *261*, 350–366. https://doi.org/10.1016/j.epsl.2007.06.032

Lim, Y. C., Lin, S., Yang, T. F., Chen, Y. G., & Liu, C. S. (2011). Variations of methane induced pyrite formation in the accretionary wedge sediments offshore southwestern Taiwan. *Marine and Petroleum Geology*, *28*, 1829–1837. https://doi.org/10.1016/j.marpetgeo.2011.04.004

Lin, A. T., Liu, C.-S., Lin, C.-C., Schnurle, P., Chen, G.-Y., Liao, W.-Z., et al. (2008). Tectonic features associated with the overriding of an accretionary wedge on top of a rifted continental margin: An example from Taiwan. *Marine Geology*, *255*, 186–203. https://doi.org/10.1016/j.margeo.2008.10.002

Liu, C.-S., Schnürle, P., Wang, Y., Chung, S.-H., Chen, S.-C., & Hsiuan, T.-H. (2006). Distribution and characters of gas hydrate offshore of southwestern Taiwan. *Terrestrial, Atmospheric and Oceanic Sciences*, *17*, 615–644. https://doi.org/10.3319/TAO.2006.17.4.615(GH)

Martín-Hernández, F., Dekkers, M. J., Bominaar-Silkens, I. M. A., & Maan, J. C. (2008). Magnetic anisotropy behaviour of pyrrhotite as determined by low- and high-field experiments. *Geophysical Journal International*, *174*, 42–54. https://doi.org/10.1111/j.1365-246X.2008.03793.x

Mineral powder diffraction file databook, sets 1–42 (1993). International Centre for Diffraction Data (ICDD), Swarthmore, Pennsylvania, U.S.A.

Morimoto, N., Gyobu, A., Mukaiyama, H., & Izawa, E. (1975). Crystallography and stability of pyrrhotites. *Economic Geology*, *70*, 824–833. https://doi.org/10.2113/gsecongeo.70.4.824

Moskowitz, B. M., Frankel, R. B., & Bazylinski, D. A. (1993). Rock magnetic criteria for the detection of biogenic magnetite. *Earth and Planetary Science Letters*, *120*, 283–300. https://doi.org/10.1016/0012-821X(93)90245-5

O'Reilly, W., Hoffman, V., Chouker, A. C., Soffel, H. C., & Menyeh, A. (2000). Magnetic properties of synthetic analogues of pyrrhotite ore in the grain size range 1–24 μm. *Geophysical Journal International*, *142*, 669–683. https://doi.org/10.1046/j.1365-246x.2000.00169.x

Özdemir, Ö., & Dunlop, D. J. (2014). Hysteresis and coercivity of hematite. *Journal of Geophysical Research: Solid Earth*, *119*, 2582–2594. https://doi.org/10.1002/2013JB010739

Pike, C. R., Roberts, A. P., & Verosub, K. L. (1999). Characterizing interactions in fine magnetic particle systems using first order reversal curves. *Journal of Applied Physics*, *85*, 6660–6667.

Pósfai, M., & Dódony, I. (1990). Pyrrhotite superstructures. Part I: Fundamental structures of the NC ($N = 2, 3, 4$ and 5) type. *European Journal of Mineralogy*, *2*, 525–528. https://doi.org/10.1127/ejm/2/4/0525

Pósfai, M., Sharp, T., & Kontny, A. (2000). Pyrrhotite varieties from the 9.1 km deep borehole of the KTB project. *American Mineralogist*, *85*, 1406–1415. https://doi.org/10.2138/am-2000-1009

Powell, A. V., Vaqueiro, P., Knight, K. S., Chapon, L. C., & Sánchez, R. D. (2004). Structure and magnetism in synthetic pyrrhotite Fe_7S_8: A powder neutron-diffraction study. *Physical Review B*, *70*, 014415.

Roberts, A. P. (1995). Magnetic properties of sedimentary greigite (Fe_3S_4). *Earth and Planetary Science Letters*, *134*, 227–236. https://doi.org/10.1016/0012-821X(95)00131-U

Roberts, A. P. (2015). Magnetic mineral diagenesis. *Earth-Science Reviews*, *151*, 1–47. https://doi.org/10.1016/j.earscirev.2015.09.010

Roberts, A. P., Chang, L., Rowan, C. J., Horng, C.-S., & Florindo, F. (2011). Magnetic properties of sedimentary greigite (Fe_3S_4): An update. *Reviews of Geophysics*, *49*, RG1002. https://doi.org/10.1029/2010RG000336

Roberts, A. P., Florindo, F., Larrasoaña, J. C., O'Regan, M. A., & Zhao, X. (2010). Complex polarity pattern at the (former) Plio-Pleistocene global stratotype section at Vrica (Italy): Remagnetization by magnetic iron sulphides. *Earth and Planetary Science Letters*, *292*, 98–111.

Roberts, A. P., Heslop, D., Zhao, X., & Pike, C. R. (2014). Understanding fine magnetic particle systems through use of first-order reversal curve diagrams. *Reviews of Geophysics*, *52*, 557–602. https://doi.org/10.1002/2014RG000462

Roberts, A. P., Liu, Q., Rowan, C. J., Chang, L., Carvallo, C., Torrent, J., & Horng, C.-S. (2006). Characterization of hematite (α-Fe_2O_3), goethite (α-FeOOH), greigite (Fe_3S_4), and pyrrhotite (Fe_7S_8) using first-order reversal curve diagrams. *Journal of Geophysical Research*, *111*, B12S35. https://doi.org/10.1029/2006JB004715

Roberts, A. P., Pike, C. R., & Verosub, K. L. (2000). First-order reversal curve diagrams: A new tool for characterizing the magnetic properties of natural samples. *Journal of Geophysical Research*, *105*, 28,461–28,475.

Robinson, P., Harrison, R. J., McEnroe, S. A., & Hargraves, R. B. (2002). Lamellar magnetism in the haematite-ilmenite series as an explanation for strong remanent magnetization. *Nature*, *418*, 517–520.

Rochette, P., Fillion, G., Ballou, R., Brunet, F., Ouladdiaf, B., & Hood, L. (2003). High pressure magnetic transition in pyrrhotite and impact demagnetization on Mars. *Geophysical Research Letters*, *30*(13), 1683. https://doi.org/10.1029/2003GL017359

Rochette, P., Fillion, G., Mattéi, J.-L., & Dekkers, M. J. (1990). Magnetic transition at 30–34 K in Fe_7S_8: Insight into a widespread occurrence of pyrrhotite in rocks. *Earth and Planetary Science Letters*, *98*, 319–328. https://doi.org/10.1016/0012-821X(90)90034-U

Rochette, P., Lorand, J. P., Fillion, G., & Sautter, V. (2001). Pyrrhotite and the remanent magnetization of SNC meteorites: A changing perspective on Martian magnetism. *Earth and Planetary Science Letters*, *190*, 1–12. https://doi.org/10.1016/S0012-821X(01)00373-9

Rochette, P., Mathé, P. E., Esteban, L., Rakoto, H., Bouchez, J. L., Liu, Q. S., & Torrent, J. (2005). Non-saturation of the defect moment of goethite and fine-grained hematite up to 57 teslas. *Geophysical Research Letters*, *32*, L22309. https://doi.org/10.1029/2005GL024196

Rudmin, M., Roberts, A. P., Horng, C.-S., Mazurov, A., Savinova, O., Ruban, A., et al. (2018). Ferrimagnetic iron sulphide formation and methane venting across the Paleocene-Eocene thermal maximum in shallow marine sediments, ancient west Siberian Sea. *Geochemistry, Geophysics, Geosystems*, *19*, 21–42. https://doi.org/10.1002/2017GC007208

Stoner, E. C., & Wohlfarth, E. P. (1948). A mechanism of magnetic hysteresis in heterogeneous alloys. *Philosophical Transactions of the Royal Society of London*, *A240*, 599–642. https://doi.org/10.1098/rsta.1948.0007

Till, J. L., Guyodo, Y., Lagroix, F., Morin, G., & Ona-Nguema, G. (2015). Goethite as a potential source of magnetic nanoparticles in sediments. *Geology*, *43*, 75–78. https://doi.org/10.1130/G36186.1

Torii, M., Fukuma, K., Horng, C.-S., & Lee, T.-Q. (1996). Magnetic discrimination of pyrrhotite- and greigite-bearing sediment samples. *Geophysical Research Letters*, *23*, 1813–1816. https://doi.org/10.1029/96GL01626

van der Zee, C., Roberts, D. R., Rancourt, D. G., & Slomp, C. P. (2003). Nanogoethite is the dominant reactive oxyhydroxide phase in lake and marine sediments. *Geology*, *31*, 993–996. https://doi.org/10.1130/G19924.1

van Dongen, B. E., Roberts, A. P., Schouten, S., Jiang, W.-T., Florindo, F., & Pancost, R. D. (2007). Formation of iron sulfide nodules during anaerobic oxidation of methane. *Geochimica et Cosmochimica Acta*, *71*, 5155–5167. https://doi.org/10.1016/j.gca.2007.08.019

Vasiliev, I., Dekkers, M. J., Krijgsman, W., Franke, C., Langereis, C. G., & Mullender, T. A. T. (2007). Early diagenetic greigite as a recorder of the palaeomagnetic signal in Miocene-Pliocene sedimentary rocks of the Carpathian foredeep (Romania). *Geophysical Journal International*, *171*, 613–629.

Wang, H., & Salveson, I. (2005). A review on the mineral chemistry of the non-stoichiometric iron sulfide, $Fe_{1-x}S$ ($0 \leq x \leq 0.125$): Polymorphs, phase relations and transition, electronic and magnetic structures. *Phase Transitions*, *78*, 547–567. https://doi.org/10.1080/01411590500185542

Weaver, R., Roberts, A. P., & Barker, A. J. (2002). A late diagenetic (syn-folding) magnetization carried by pyrrhotite: Implications for paleomagnetic studies from magnetic iron sulphide-bearing sediments. *Earth and Planetary Science Letters*, *200*, 371–386. https://doi.org/10.1016/S0012-821X(02)00652-0

Wehland, F., Stancu, A., Rochette, P., Dekkers, M. J., & Appel, E. (2005). Experimental evaluation of magnetic interaction in pyrrhotite bearing samples. *Physics of the Earth and Planetary Interiors*, *153*, 181–190. https://doi.org/10.1016/j.pepi.2005.05.006

Zhao, X., Roberts, A. P., Heslop, D., Paterson, G. A., Li, Y. L., & Li, J. H. (2017). Magnetic domain state diagnosis using hysteresis reversal curves. *Journal of Geophysical Research: Solid Earth*, *122*, 4767–4789. https://doi.org/10.1002/2016JB013683